









## Magnetic field re-configuration associated with a slow rise eruptive X1.2 flare in NOAA active region 11944

VASYL YURCHYSHYN <sup>1</sup>, XU YANG <sup>1</sup>, GELU NITA <sup>2</sup>, GREGORY FLEISHMAN <sup>2,3</sup>, VALENTINA ABRAMENKO <sup>4</sup>,  
SATOSHI INOUE <sup>2</sup>, EUN-KYUNG LIM <sup>5</sup>, AND WENDA CAO <sup>1</sup>

<sup>1</sup>*Big Bear Solar Observatory, New Jersey Institute of Technology,  
40386 North Shore Lane, Big Bear City, CA 92314, USA*

<sup>2</sup>*Center for Solar-Terrestrial Research, New Jersey Institute of Technology,  
323 M.L. King Jr. Blvd., Newark, NJ 07102-1982, USA*

<sup>3</sup>*Ioffe Institute, Polytekhnicheskaya, 26, St. Petersburg, 194021, Russia*

<sup>4</sup>*Crimean Astrophysical Observatory of Russian Academy of Science, Nauchny, Bakhchisaray, Russia*

<sup>5</sup>*Korea Astronomy and Space Science Institute, Daedeokdae-ro 776, Yuseong-gu. Daejeon 34055, Republic of Korea*

(Received February 19, 2022; Revised February 19, 2022; Accepted February 19, 2022)

Submitted to *Frontiers in Astronomy*

### ABSTRACT

Using multi-wavelength observations, we analysed magnetic field variations associated with a gradual X1.2 flare that erupted on January 7, 2014 in active region (AR) NOAA 11944 located near the disk center. A fast coronal mass ejection (CME) was observed following the flare, which was noticeably deflected in the south-west direction. A chromospheric filament was observed at the eruption site prior to and after the flare. We used SDO/HMI data to perform non-linear force-free field (NLFFF) extrapolation of coronal magnetic fields above the AR and to study the evolution of AR magnetic fields prior to the eruption. The extrapolated (model) data allowed us to detect signatures of several magnetic flux ropes (MFRs) present at the eruption site several hours before the event. The eruption site was located under slanted sunspot fields with a varying decay index of 1.0-1.5. That might have caused the erupting fields to slide along this slanted magnetic boundary rather than vertically erupt, thus explaining the slow rise of the flare as well as the observed direction of the resulting CME. We employed sign-singularity tools to quantify the evolutionary changes in the model twist and observed current helicity data, and found rapid and coordinated variations of current systems in both data sets prior to the event as well as their rapid exhaustion after the event onset.

*Keywords:* Sun: corona — Sun: flares — Sun: magnetic fields — Sun: activity

### 1. INTRODUCTION

Coronal Mass Ejections (CMEs) have long been identified as a prime cause of large, non-recurrent geomagnetic storms (e.g., Burlaga et al. 1981; Tsurutani et al. 1988; Gosling et al. 1990; Zhang et al. 2007). Solar plasma and magnetic fields ejected into the heliosphere as a result of an eruption are further propelled into interplanetary space where they may encounter the Earth’s magnetosphere and produce large southward excursions of the interplanetary magnetic field. Interplanetary CMEs observed near the Earth often exhibit a flux rope structure (e.g., Burlaga et al. 1981; Marubashi et al. 2015), meaning that they harbor a large-scale, coherent loop-like structure with a large amount of twist. Many studies have illustrated that the sense of the magnetic twist and the direction of the fields in ICMEs matches those of the source region, thus opening a pathway for predicting the likelihood of geomagnetic storms (e.g., Pevtsov & Canfield 2001; Yurchyshyn et al. 2005; Gopalswamy et al. 2007; Marubashi et al. 2015, and references therein) and

the CME speed may be related to the magnitude of the associated storm (e.g., Yurchyshyn et al. 2004; Srivastava & Venkatakrishnan 2004; Yurchyshyn et al. 2005).

CMEs most frequently erupt from solar active regions (ARs) and are often accompanied by solar flares (Zhang et al. 2007). During an eruption event, stored free energy is released from complex magnetic structures of an AR through series of magnetic reconnections. While current CME models commonly assume the presence of a magnetic flux rope (MFR) in the ejecta, they differ in the way the initiation of the eruption is treated. In some models, an MFR is required to exist prior to the eruption (e.g., Chen & Shibata 2000; Fan & Gibson 2004; Török & Kliem 2005; Kliem & Török 2006), while in other models the eruption begins from reconnection in a sheared magnetic arcade (SMA) and an unstable MFR is formed in the process of the event (Antiochos et al. 1999; Moore et al. 2001; Karpen et al. 2012). Meanwhile, some studies also discussed borderline cases, when the detailed topological analysis reveals weakly twisted MFRs, and field line plots show the presence of an SMA (Aulanier et al. 2009; Savcheva et al. 2012). More details on pre-eruptive magnetic configurations may be found in a recent comprehensive review by Patsourakos et al. (2020). Real life eruptions may not follow any particular eruption model and studies of pre-eruptive magnetic fields are vital for understanding and predicting solar eruptions.

Solar ARs present various magnetic structures and topologies and some of them are prone to eruption (e.g., Kusano et al. 2012; Toriumi et al. 2017a). One of the global goals of solar physics is to understand how an AR evolves toward eruption. From a practical point of view, we would like to know where and when the next eruption will occur. Most of the modern forecasting research (e.g., Falconer et al. 2014; Barnes et al. 2016; Leka et al. 2019a,b) is based on analysis of observed photospheric magnetograms provided by Helioseismic and Magnetic Imager (HMI) instrument (Scherrer et al. 2012; Schou et al. 2012) on board Solar Dynamics Observatory (SDO, Pesnell et al. 2012). However, photospheric measurements alone do not uniquely represent the complexity of coronal magnetic fields rooted in the photosphere, which is of vital importance for understanding the eruption process. Energy needed to expel twisted magnetic structures and plasma in the interplanetary space is stored in the corona above an AR is thought to be generated by plasma flows in the photosphere and the convection zone. Moreover, structural organization of the coronal fields is also responsible for the initiation of eruption, since their continuous evolution may lead to an unstable state, when the force balance is disrupted and the a MFR or a SMA may erupt.

Several studies took advantage of the advances in modeling of AR coronal fields and used modeling results address flare forecasting by analyzing, for example, pre-flare magnetic energy balance (e.g., Gupta et al. 2021), the rate of decay of coronal fields (e.g., Jing et al. 2018), and determining the pre-eruptive configuration (e.g., Duan et al. 2019a; Kusano et al. 2020). A recent comprehensive comparison of flare forecasting methods is given in Park et al. (2020).

Here we use series of non-linear force-free field (NLFFF) extrapolations to explore evolution of an AR configuration toward an eruptive state. We analyze the model configurations using twist and q-factor maps (Titov et al. 2002; Titov 2007; Liu et al. 2016) and their complexity is measured by using a cancellation exponent (e.g., Ott et al. 1992; Yurchyshyn et al. 2000a) and the decay index (Kliem & Török 2006).

## 2. DATA AND METHODS

We use HMI magnetic field measurements as a boundary condition to perform the magnetic field extrapolation. HMI observes the full solar disk in the Fe I 617.3 nm absorption line with a spatial resolution of  $1''$ . To generate the photospheric level vector magnetic field boundary conditions, we used HMI data rebinned to 1 Mm pixel scale transformed to a local Cartesian coordinate system using the same Cylindrical Equal Area (CEA) projection (Thompson 2006) used to produce the standard *hmi.sharp\_cea\_720s* series data (SHARP, Bobra et al. 2014). Our customized coordinate transformations use a reference point exactly centered on the base of the Cartesian box to ensure that when the model is placed in the proper 3D orientation relative to the observer, the base maps are projected onto their line-of-sight (LOS) counterparts with minimum distortion.

Atmospheric Imaging Assembly (AIA, Lemen et al. 2012) provides full-disk images of the solar corona in a broad UV range nearly simultaneously with an image scale of  $0''.6$  per pixel and a cadence of 12 s covering a wide and nearly continuous coronal temperature range of 0.7–20 MK. AIA 17.1 and 160 nm images were used to determine timing and location of initial flare brightenings as well as to verify the coronal field extrapolation results.

### 2.1. Coronal Field Extrapolation

Coronal field extrapolation was performed using Fleishman et al. (2017) tool that exploits the optimization method developed by Wheatland et al. (2000). An optimization method allows us to transform an initial magnetic configuration

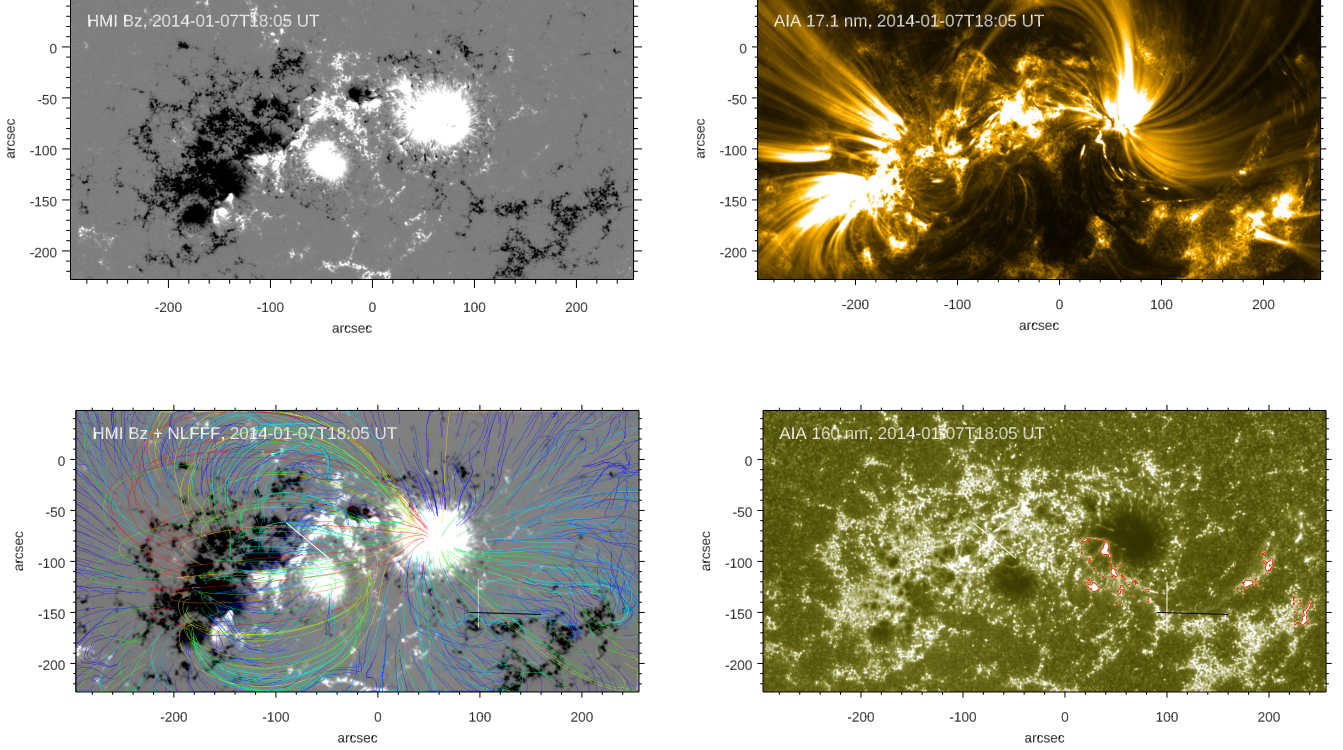


**Figure 1.** NOAA AR 11944 as it appeared in an HMI magnetogram (top left) as well as AIA 17.1 nm and 160 nm imaging data (top right, bottom right) on 7 January 2014 at 18:05 UT. The bottom left panel shows the same HMI magnetogram overplotted with the results of magnetic field extrapolation. Color coding of field lines indicates their length (blue - shortest, red - longest).

to a final non-linear force-free field (NLFFF) configuration. Fleishman et al. (2017) method follows an approach of using the weight function presented in Wiegmann (2004). Authors modified the original method so that no pre-processing of the photospheric boundary conditions is performed and the initial approximation for the magnetic field for the most sparse grid is the potential field, while for each next, denser grid, the initial field is taken as an appropriate interpolation of the final (NLFFF) state of the previous grid. The numerical realization of this approach is part of the *GX Simulator* package (Nita et al. 2015, 2018), which is freely available from the *SolarSoft* IDL library.

## 2.2. Magnetic Flux Rope Identification Approach

Coronal field extrapolations allow us to search for possible signatures of a MFR using the squashing factor,  $Q$ , and magnetic twist,  $T_W$ , parameters calculated inside the extrapolated volume (Titov et al. 2002; Titov 2007; Liu et al. 2016). The definitions of an MFR found in literature are not very strict and often magnetic twist (Berger & Prior 2006) is used as a discriminator to identify a MFR. This parameter defines the number of turns that two close field lines make around each other and it is often accepted that a MFR is an ensemble of field lines with a twist exceeding unity. Here we adopt the definition of a MFR presented in Patsourakos et al. (2020). A MFRs is a twisted structure with a magnetic axis that follows a PIL, a current channel, and twist extending over the full length of the magnetic axis. MFRs are not expected to exhibit uniform twist along the entire length. It was also suggested that when a MFR is twisted in excess of a critical value  $T_{Wc} > 1.25$ , kink instability may develop leading to a subsequent eruption (e.g., Hood & Priest 1981; Baty 2001; Török & Kliem 2003; Fan & Gibson 2003). Generally speaking, MFRs are associated with the presence of extended, often line-shaped high  $Q$ -structures located near a polarity inversion line (PIL) (Liu et al. 2016). Hereinafter we will refer to them as high  $Q$ -lines. It should be noted however, that not every strong  $Q$ -lane indicates the presence of a MFR, since short  $Q$  lines also may appear in connection with SMAs. Strong  $Q$ -lanes may be viewed as the photospheric footprint of quasi-separatrix layers (QSL) which are the interface between two magnetic flux systems. They are known to display a strong connectivity gradient (Titov et al. 2002; Titov 2007; Liu et al. 2016).



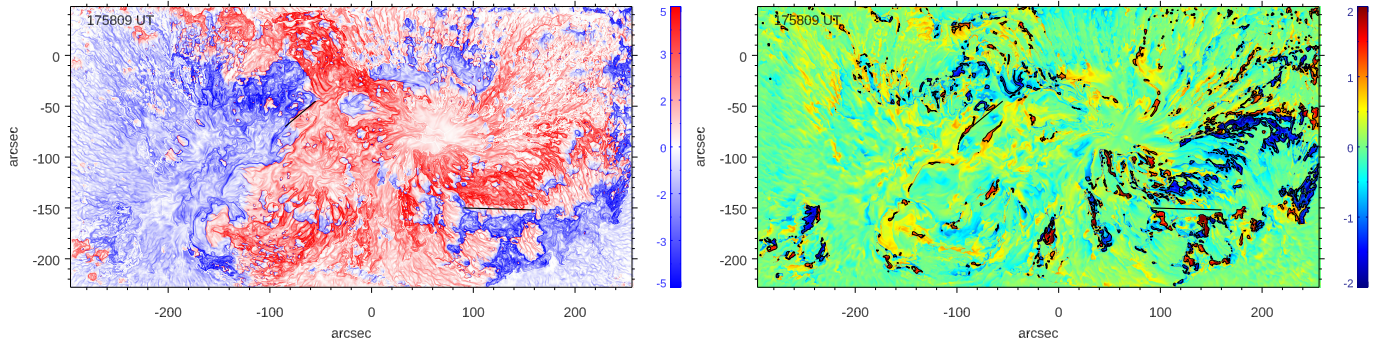


**Figure 2.** Distribution of  $\log Q$  (left) and  $T_W$  parameters on the photosphere immediately before the flare onset. The two line segments in the maps mark strong Q-lanes situated above the photospheric polarity inversion line. The images are scaled between  $-2 < T_W < 2$ , while contours outline areas with  $|T_W| > 1$ . Contours in the  $T_W$  map outline  $\pm 1$  twist patches.

### 3. RESULTS

In Figure 1 we show an HMI magnetogram (top left), AIA 17.1 (top right) and 160 nm (bottom right) images, and results of the coronal field extrapolation plotted over the HMI magnetogram. Contours in the AIA 160 nm panel outline initial brightenings associated with an X1.2 flare that erupted on 2014 January 7 at 18:04 UT, peaked at 18:32 UT and ended at 18:58 UT. This was a slow rise flare followed by a fast CME and a coronal wave. We note that the first short lived and compact brightenings (flare precursors) appeared at the site of eruption about 20 minutes prior to the flare onset indicating on possible pre-flare activity at this location. This event was at the focus of two case (Wang et al. 2015; Zheng et al. 2016) and several statistical (Falconer et al. 2016; Toriumi et al. 2017b; Toriumi & Takasao 2017; Lu et al. 2019; Duan et al. 2019b, 2021) studies. The flare erupted at the outskirts of the AR, south-west of the leading sunspot and away from the major PIL. Zheng et al. (2016) noted a complex structure of flare ribbons located on both sides of a chromospheric filament. One of the ribbons was visible for about 3 hours after the flare onset and it is worth noting that the  $H\alpha$  filament was visible at that moment as well<sup>1</sup>.

The magnetic field extrapolation results produced by the GX method (Figure 1, lower left panel) show that the AR had a bipolar configuration with the following part nearly entirely connected to a fraction of the leading sunspot. The rest of the leading magnetic flux appeared to be connected to surrounding plage fields and part of it spanned the eruption site.

To estimate whether the extrapolated fields satisfactorily describe the observed fields we followed approach suggested by Yardley et al. (2021), who considered model results to be a good match to the data if the model reproduces the main coronal features (loops, filaments and sheared structures). Moreover, in case an eruption was observed in an AR, the model should be able to satisfactorily reflect the build-up to the eruption as well as the post-eruption/flare changes. The comparison of AIA 17.1 nm images and the line plot shows that the extrapolations satisfactorily describe the large-scale configuration of the AR. Although there is distinction between the shape of AIA 17.1 nm and model loops in the center of the FOV, they still are rooted in approximately the same area on the Sun. Next, the field line plot also highlighted two segments of the PIL centered at  $(110'', -160'')$  and  $(-90'', -70'')$ , with a strong vertical shear in the magnetic field, i.e., shorter, deeper field lines (blue) are nearly orthogonal to the overlaying fields (green). The first, western PIL segment at  $(110'', -160'')$  was associated with the X1.2 flare, while the second, eastern segment was associated with frequent small-scale brightenings observed several hours before and during the X1.2 flare. The two PIL segments were co-spatial with regions of strong shear in the AR, which increases the reliability of the extrapolated fields. Finally, we will show further in the text that evolution of the extrapolated fields is consistent with the observed activity in the AR.

Figure 2 shows the corresponding **signed logarithmic**  $Q$  and  $T_W$  maps derived from an extrapolated data cube. The two segments of the PIL discussed above are indicated by solid lines. The flaring PIL in the lower right corner of the  $Q$  map is enclosed by extended areas of high  $Q$  values of opposite sign suggesting strong magnetic shear. The

<sup>1</sup> <ftp://gong2.nso.edu/HA/hag/201401/20140107/>



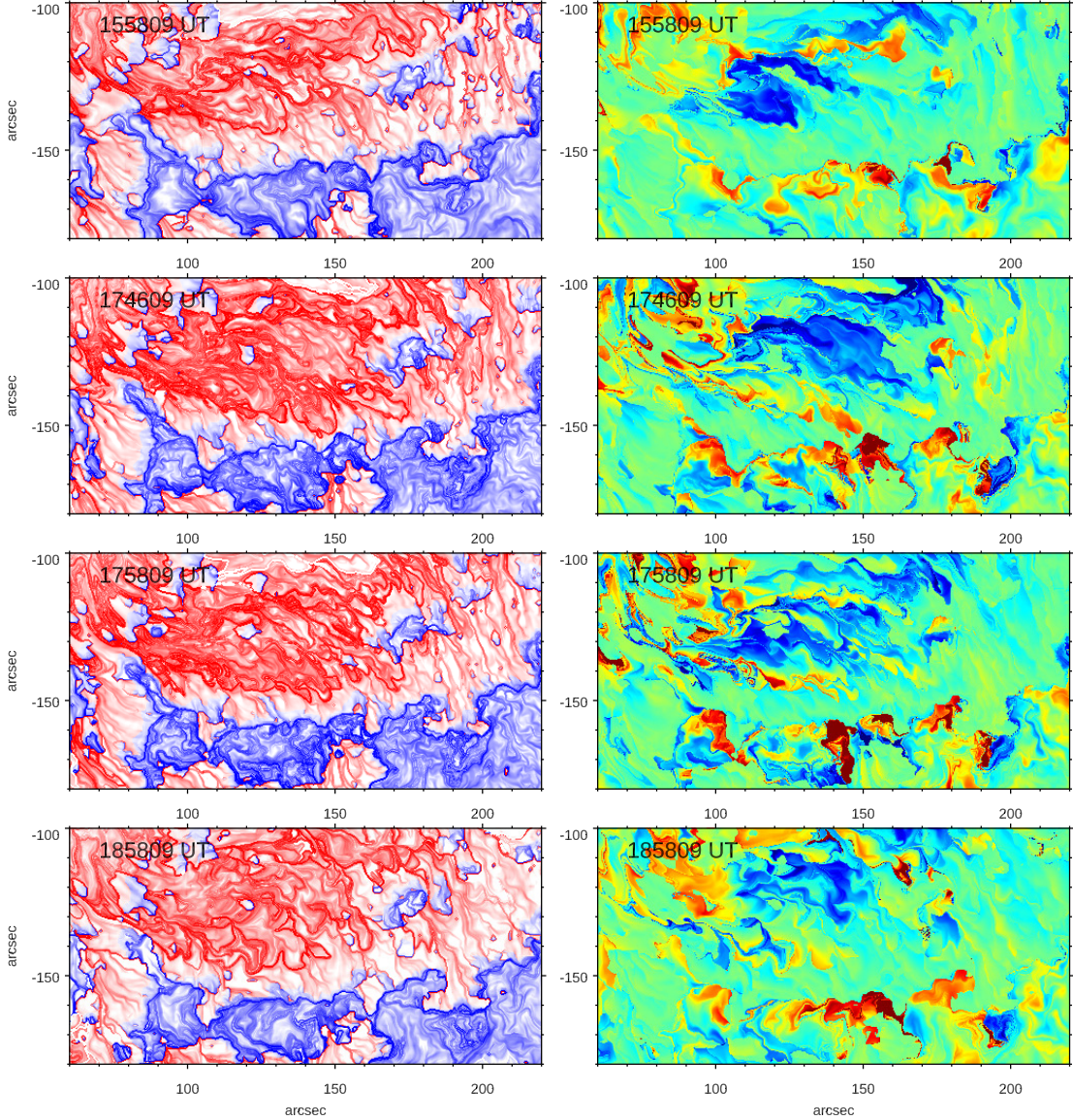


**Figure 3.** Evolution of  $Q$  (left) and  $T_W$  parameters near the flaring PIL. Twist maps are scaled between  $\pm 2$  units.

eastern PIL is also associated with high  $Q$  values although it is not as extended as the flaring one. It is also worth noting that in general the  $Q$  parameter is highly structured as evidenced by a network of high  $Q$ -lines indicating high degree of filamentation of the magnetic field and associated current systems. The twist map (right panel) shows that, unlike the rest of the AR, strongly twisted extended structures are present on both sides of the flaring PIL segment and negative (positive) twist dominates over the area north (south) of the flaring PIL segment. Since this PIL was at the origin of the eruptive flare we show the pre-flare evolution of  $Q$  and  $T_W$  parameters near the PIL in detail (Figure 3). The  $T_W$  maps show that between 16:00 UT and 17:46 UT the twist has significantly enhanced, while the  $Q$  maps show development and enhancement of multiple strong  $Q$ -lanes, which indicates enhancement and fragmentation of electric currents. The low  $Q$  corridor ( $y=-150''$ ,  $x=90-180''$ ) that separates the negative (red) and positive (blue)  $Q$  areas has narrowed and nearly vanished at  $(150'', -153'')$  in the 17:46:09 UT panel, when a strong twist structure developed at that location. Narrowing of the weak  $Q$ -lane indicates convergence of magnetic structures and possible rise of coronal magnetic fields above the PIL.

To explore the evolution of coronal fields above the flaring PIL, we calculated  $T_W$  maps (Figure 4) at a vertical plane crossing the system of intertwining lines in its mid-section ( $x=100$ ,  $y=-120$  —  $-170$ , see white vertical line in Figure 1). The leading sunspot was located to the left of the FOV ( $x=-15''$ ) and the sunspot field manifested itself in the upper

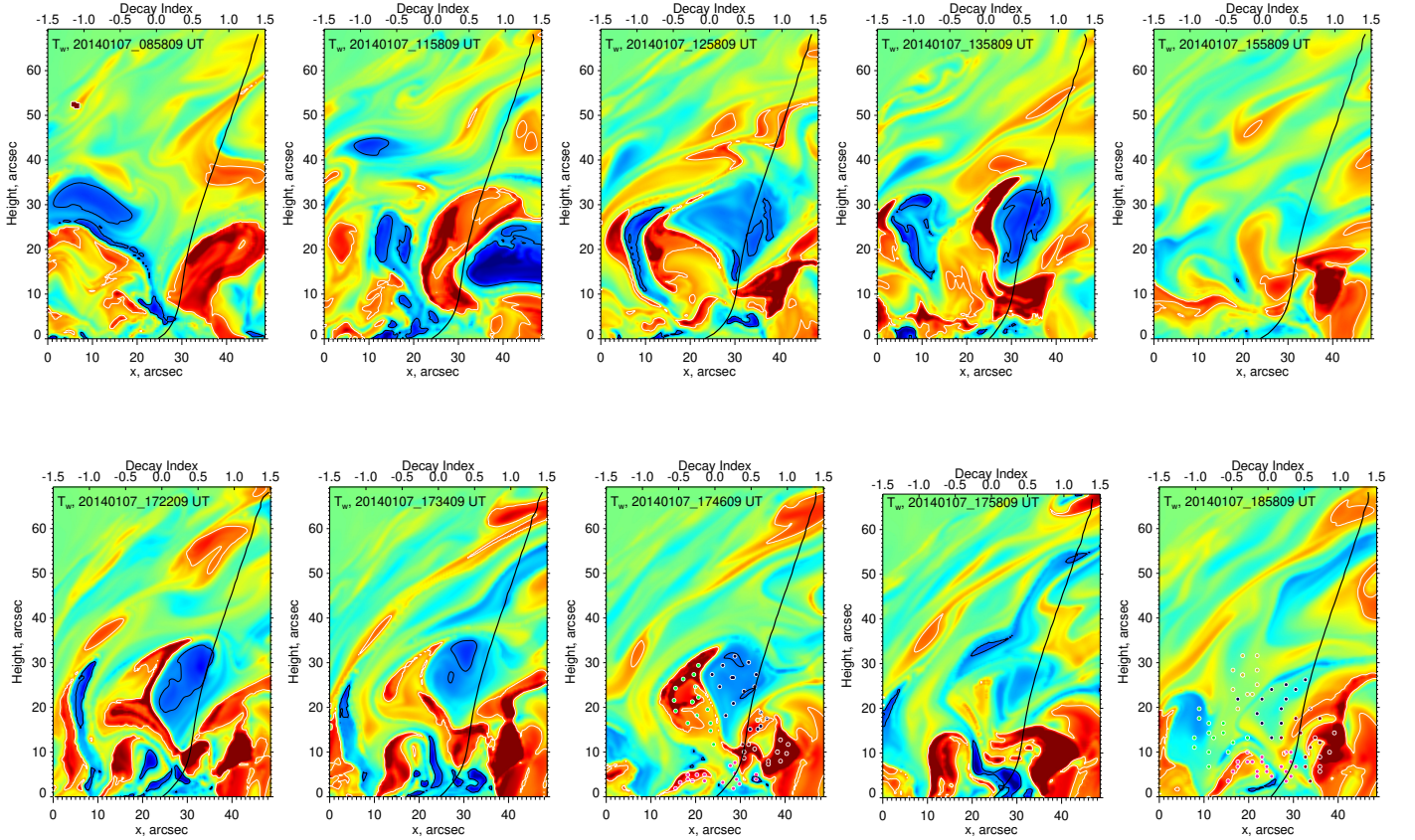


**Figure 4.** Field line twist,  $T_W$ , maps shown for several instances for the west flux rope (FR). The  $T_W$  was calculated on a vertical plane orthogonal to the axis of an eruptive AR filament. The images are scaled between  $-2 < T_W < 2$ , while contours outline areas with  $|T_W| > 1$ . The black curve is the decay index profile calculated along the flaring PIL at  $x=25''$ . The x-axis begins at the top end of the cross-section (Fig. 1) and the sunspot is outside the FOV on the left side of the panels. The y-axis is represents the height above the photosphere. The color coded dots in 17:46:09 and 18:58:09 UT panels indicate the locations through which we traced the fields lines shown in Fig. 5.

part of the panels as diagonally slanted narrow islands of positive and negative twist patches. There were two time intervals (09:00-16:00 UT and 16:00-19:00 UT) during which various large twist structures formed and disappeared. About 2 hs prior to the flare (15:58:09 UT panel) there were no strong twist structures present above the PIL located at  $x=25''$ , and only one positive  $T_W$  patch was detected  $\approx 10''$  above the photosphere south of the PIL at  $x=39''$ . Note, that the origin of the x-axis is at the upper tip of the white line segment in Figure 1. According to the 17:46:09 UT panel in Figure 4, this structure at that time significantly weakened which is also reflected in the narrowing of the weak Q-corridor discussed above. By 17:20 UT a patch of  $T_W > 1$  (blue) has developed in the center of the FOV surrounded by an extended area of positively twisted fields (red). It was later (17:58 UT) seen weakened and elongated as it was rising up into the corona. At the same time, many strongly twisted structures seen below  $y=10''$  in the 17:58 UT panel have disappeared from the FOV as well. We also note that the strongly positively twisted structure with  $T_W > 2$  seen at  $(40'', 10'')$  observed at 16:00 UT remained stationary during as well as after the eruption.

In Figure 5 we show line plots for the pre (17:46 UT, top) and post (18:58 UT, bottom) models. Different colors indicate different magnetic flux systems. The choice of plotted field lines was dictated by the twist structures shown in the 17:46:09 UT and 18:58:09 UT panels in Figure 4. To visualize the 3D structures associated with the 2D twist patches we manually selected pixels in these panels through which we intended to trace field lines. As a rule, the pixels were selected to outline twist patches of interests including several trace points within a patch. Thus, the white-blue colored field lines in panel c are those that pass through the negative (blue)  $T_W$  patch centered at  $(30'', 25'')$  in the 17:46:09 UT panel, while the green colored lines are associated with the positive (red) patch at  $(20'', 23'')$ . Similarly,



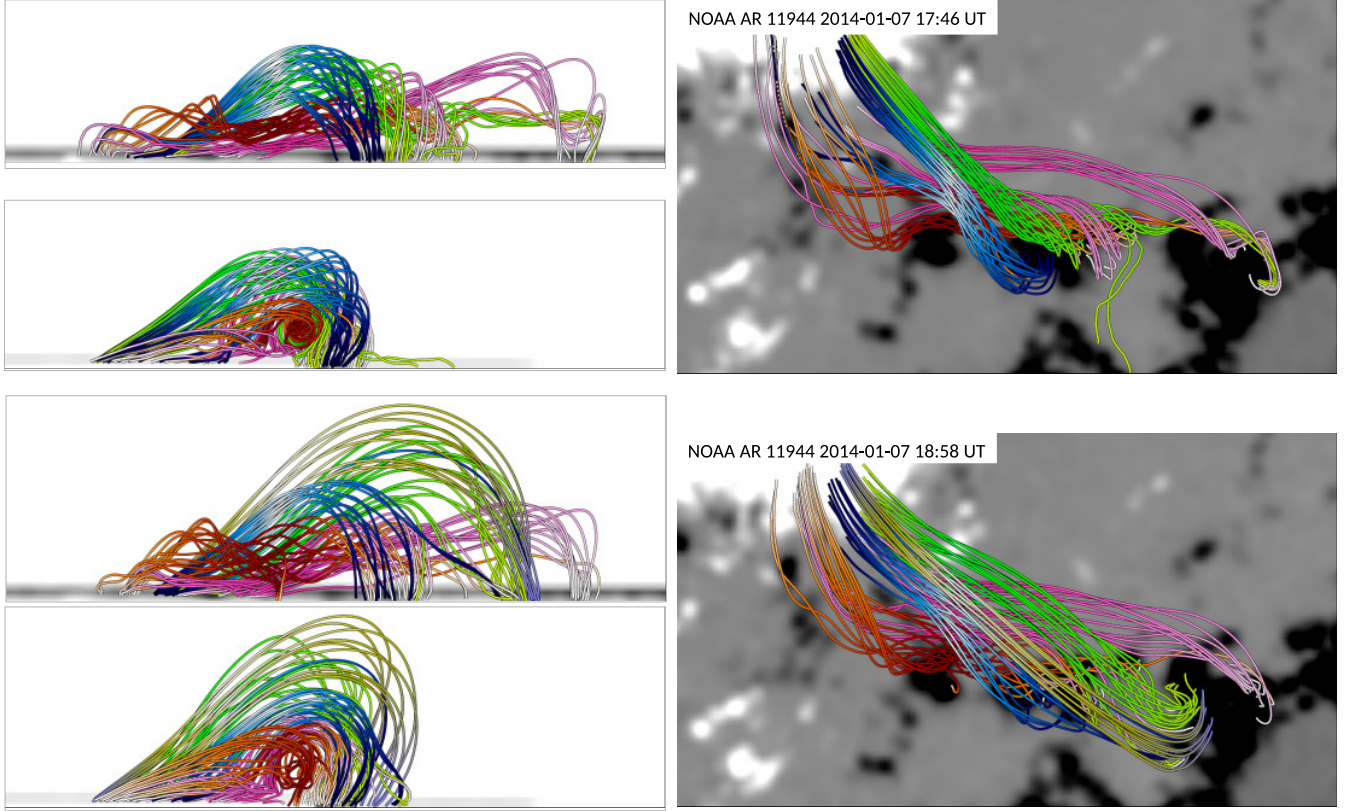


**Figure 5.** Results of magnetic field extrapolation using a pre-flare (17:46 UT, top) and post-flare (18:58 UT, bottom) magnetic field measurements. The FOV shown is  $140'' \times 70'' \times 70''$  and is located at  $55 < x < 220$  and  $-180 < y < -80$  in Figure 1. Colored lines highlight various magnetic flux systems associated with the twist strictures shown in Fig. 4.

the dark red lines are associated with the strong positive  $T_W$  at  $(40'', 10'')$  and the purple lines are those passing through two small scale patches seen below  $10''$ . The left column of panels show side views of the same line plot. Panel b (axis view) shows that most of the red field lines make at least one turn, although when inspecting all panels together one may arrive to a conclusion that some of the red lines make two turns: first they dip and turn under the green and orange lines in the right side of the panels and then they make another turn in the left side of the panel. Some of the green lines, too, dip and turn under the orange and red lines and then continue as a large loop. They (green lines) are also seen in panel b making a full turn. The pink lines appear be less twisted and only some of them are likely to make one turn, thus representing a weakly twisted MFR (Patsourakos et al. 2020). The bottom set of panels in Figure 5 show the field lines extrapolated using an after-flare 18:58:09 UT HMI magnetogram. The flare-related reconfiguration of the magnetic fields is evident in both the twist and the line plot images. The only structure least affected by the flare is the MFR seen at  $(40'', 10'')$  in the  $T_W$  panel (dark red lines). The overlying fields (blue, green) seemingly changed their connectivity and appear now less twisted, while the twisted bundle of green, red and purple lines in the center of the upper-right panel and the corresponding  $T_w$  structures have disappeared and the overall configuration became more relaxed. These extrapolation results suggest that the photosphere “sensed” the eruption which manifested itself in restructuring of coronal fields.

### 3.1. Decay Index and Critical Twist

Development of torus instability is mainly governed by the large-scale fields that straddle and stabilize a MFR. When the overlying fields sufficiently rapidly weaken with height, a MFR may become unstable and eruption may be initiated. The rate of decrease may be described by the decay index,  $n = -d\log(B_{ext})/d\log(h)$  where  $B_{ext}$  and  $h$  are



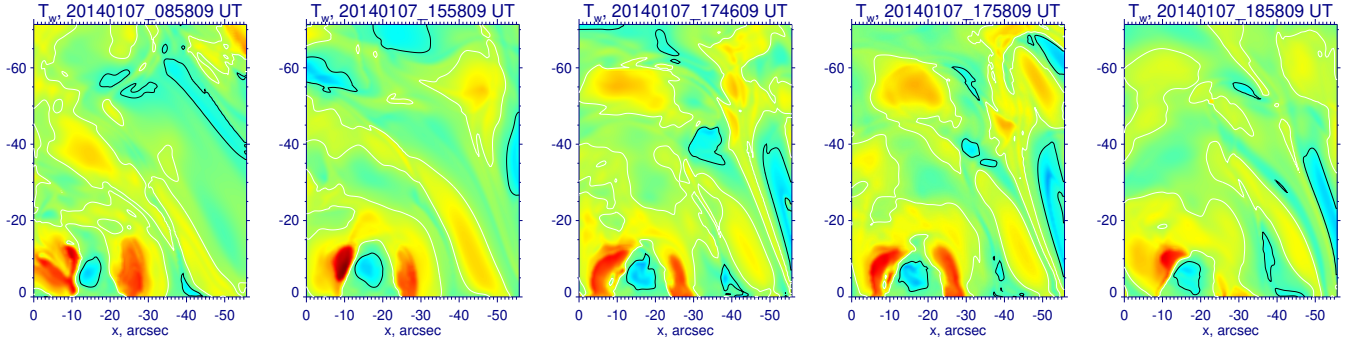


**Figure 6.** Field line twist,  $T_W$ , maps shown for several instances for the east flux rope (FR). The  $T_W$  was calculated on a vertical plane orthogonal to the eastern PIL. The images are scaled between  $-2 < T_W < 2$ , while contours outline areas with  $|T_W| > 1$ . The x-axis begins at the upper-left end of the cross-section (Fig. 1) and the sunspot is outside the FOV on the right side of the panels. The y-axis is represents the height above the photosphere in arcseconds.

external potential field and height, (Kliem & Török 2006), and it was suggested that configurations with  $n \geq 1.5$  are prone to torus instability (e.g., Török & Kliem 2005; Aulanier et al. 2010). Following studies, however, reported that there may be a wide range of the eruption threshold values,  $0.5 < n < 2$ , (e.g., Fan & Gibson 2007; Démoulin & Aulanier 2010; Olmedo & Zhang 2010; Zuccarello et al. 2015; Jing et al. 2018).

In Figure 4 decay index profiles are plotted over the  $T_w$  images. The profiles were obtained by averaging individual profiles calculated along the line shown in Figures 1 and 2 using potential field extrapolations. Instead of using the total perpendicular component of the potential field, we followed Kliem et al. (2021) recommendation and calculated the decay index only using the poloidal component of the potential field, which in our case, corresponds to the  $B_y$  component since the PIL runs parallel to the x-axis of the magnetogram. We should note though that we did calculate the decay index using the total horizontal field, and found that while there were no significant changes in the shape of the profiles, the values of the decay index were somewhat lower. The profiles show that the index began its steady decline at heights of about  $23''$ . However, its value remained below 1.5 level prior to and during the eruption, which is likely due to the strong sunspot fields extending above the flaring PIL. According to the model, the rising negative (blue) twist structure appeared to be sliding/escaping into the corona up and away from the leading sunspot along the sunspot field, thus suggesting that the associated coronal eruption and the CME may be deflected SW although the AR was located near the disk center. According to the CME Catalog (Yashiro et al. 2004) a massive halo CME<sup>2</sup> erupted at 18:24 UT with a linear speed of about  $1830 \text{ km/s}$  and mainly occupied the SW quadrant of the LASCO FOV, which qualitatively agrees with the above inference.

In contrast, similar  $T_W$  maps (Figure 6) made across the eastern PIL segment (see Figure 1) paint a far more stable picture where the main structural elements can be easily traced along the entire observed period. This area of the AR was associated only with frequent, short lived compact brightenings and it was not directly involved in the X1.2 flare discussed here. Nevertheless, the after flare 18:58 UT image shows that one of the positively twisted structures (red, at  $-30'', 7''$ ) has disappeared from the FOV. The striking difference between the dynamics seen in these two cross-sections is also evidence that the evolution seen in Figure 4 is not due to inherent instabilities of the method, but are rather driven by varying photospheric boundary conditions.

### 3.2. Sign-Singularity Measure

We analysed the twist images by means of the sign-singularity measure, a function that displays a linear range with a slope of  $k$ , called cancellation exponent (Ott et al. 1992; Abramenko et al. 1998; Yurchyshyn et al. 2000a; Sorriso-Valvo et al. 2004a; Yurchyshyn et al. 2012; Sorriso-Valvo et al. 2015). The dependence of the sign oscillation with spatial scale (scaling properties) can be analyzed by introducing the signed measure,  $\chi(r)$ , (Ott et al. 1992):

$$\mu_i(r) = \frac{\int_{L_i(r)} U(x, y) dx dy}{\int_{L_i(R)} U(x, y) dx dy}, \quad (1)$$

<sup>2</sup> [https://cdaw.gsfc.nasa.gov/CME\\_list/UNIVERSAL/2014\\_01/univ2014\\_01.html](https://cdaw.gsfc.nasa.gov/CME_list/UNIVERSAL/2014_01/univ2014_01.html)

where  $U(x, y)$  is a studied signed parameter, and  $L_i(r) \subset L_i(R)$  represents a unique hierarchy of disjoint squares of size  $r$ , covering the whole square  $L$  of size  $R$  that encloses an AR of a part thereof (also see Yurchyshyn et al. 2000a, for details). We can then define a scaling exponent:

$$\chi(r) = \sum_{L_i(r)} |\mu_i(r)| \sim r^{-\kappa}. \quad (2)$$

This measure allows us to analyse and qualitatively describe sign distribution and intensity fluctuations of a signed structure such as the twist images shown in Figure 4. Higher values of  $k$  (steeper measure) are only possible when the cancellations between positive and negative contributions in the sign-singularity measure (hereafter called spectrum) reduce with  $r \rightarrow 0$ , i.e., there is significant imbalance of the sign at all scales (for further discussion see Sorriso-Valvo et al. 2004b). In general, an increase of the cancellation exponent indicates that the analyzed structure became either more fragmented (rapid fluctuation of sign) and/or the sign fluctuations become more powerful.

In Figure 7 (left) we show  $\chi(r)$  spectra calculated for  $T_W$  maps shown in Figure 4. The majority of the spectra in Figure 7 (left, except the 15:58 UT spectrum) do not show one extended linear range. Instead, the spectrum breaks in two intervals at scale of about 6 Mm, allowing us to determine two exponents,  $k_T^{short} (< 6\text{Mm})$  and  $k_T^{long} (> 6\text{Mm})$ , and their variation over the observed period are shown in the right panel of Figure 7. There we also plot the total power, which is an integral of a spectrum over the entire spatial range. We see that the  $k_T^{short}$  is very small and it does not show much time variations. The short scale end of the spectra below  $< 6$  Mm appears to be nearly saturated indicating that small-scale twist (current) structures below 6 Mm are rather smooth and devoid of significant fluctuations in sign. In contrast, the  $k_T^{long}$  exponent is highly variable and is nearly synchronous with the total power, reflecting the varying height of the spectra (left panel). They both started to increase prior to a M7.2 flare that occurred in the trailing part of the AR. Although according to SDO/AIA data the M7.2 flare did not directly involve the studied area, it is worth noting that it was followed by multiple brightenings and plasma flows in the vicinity of both PILs. Nevertheless, the  $k_T^{long}$  was steadily decreasing after this activity period and reached its minimum at about 16:00 UT, which can also be evidenced in Figure 4 as the large scale twist structures disappeared from the FOV between 14:00 UT and 16:00 UT. The  $k_T^{long}$  and the total power began to increase again and peaked at about 17:30 UT, prior to the first short and compact brightenings that appeared at the eruption site. The twist images in Figure 4 show that during this time new large scale twist structures appeared, which then weakened and completely disappeared by the end of the impulsive phase of the flare (19:00 UT), which is also reflected in the  $k_T^{long}$  and total power plots.

The  $k_T^{long}$  exponent was determined from the model twist data and thus, in general, may not reflect real evolution of the AR magnetic fields. We thus utilized HMI magnetograms to calculate current helicity and the corresponding sign-singularity measures. Current helicity,  $H_c$ , defined as a product of the magnetic field and the associated electric currents. This parameter seems to be an important descriptor of energy capability of an AR (Seehafer 1994). Some general characteristics of current helicity (such as imbalance, hemispherical segregation, injection rate, etc.) have been extensively studied by several groups (e.g., Pevtsov et al. 1994; Abramenko et al. 1996; Park et al. 2020). Abramenko et al. (1998) and Yurchyshyn et al. (2000b, 2012) studies showed that there is a noticeable decrease of the cancellation exponent prior to periods of enhanced flaring.

Similarly to the twist data, the  $k_h^{short}$  exponent of current helicity (Figure 8, left) does not show strong temporal variations and remains at  $\sim 0.5$  level for most of the time. The total power and  $k_h^{long}$  exponent are synchronous and their general trend is similar to that observed for the twist parameter calculated for a vertical cross-section (Figures 4 and 7, middle). They all peak at about 12:00 UT and at about 17:45 UT. In case of the X1.2 flare the cancellation exponent and the total power began their rapid decrease prior to the flare onset, which is consistent with the earlier reported findings and suggests that the magnetic configuration experienced rapid changes prior to the impulsive phase of the flare. We thus conclude that the modeled  $T_w$  maps and observed vector magnetograms seem to exhibit the same tendency, namely, enhancement of their structure prior to the flare and their rapid exhausting that begins immediately before the onset of the impulsive phase.

In the right panel of Figure 8 we plot time variations of the total signed  $B_z$ ,  $B_x$ , and  $B_y$  flux calculated over the entire area shown in Figure 1. All six profiles exhibit coherent and gradual variations, which do not appear to be well correlated with the sign-singularity parameters showed in Figures 7-8. The cancellation exponents peak twice at about 12:00 UT and 17:40 UT, when the magnetic flux was gradually decreasing (12:00 UT) and increasing (17:40 UT), while both cancellation exponents and magnetic flux have a wide minimum at about 14:00-16:00 UT. Therefore, while

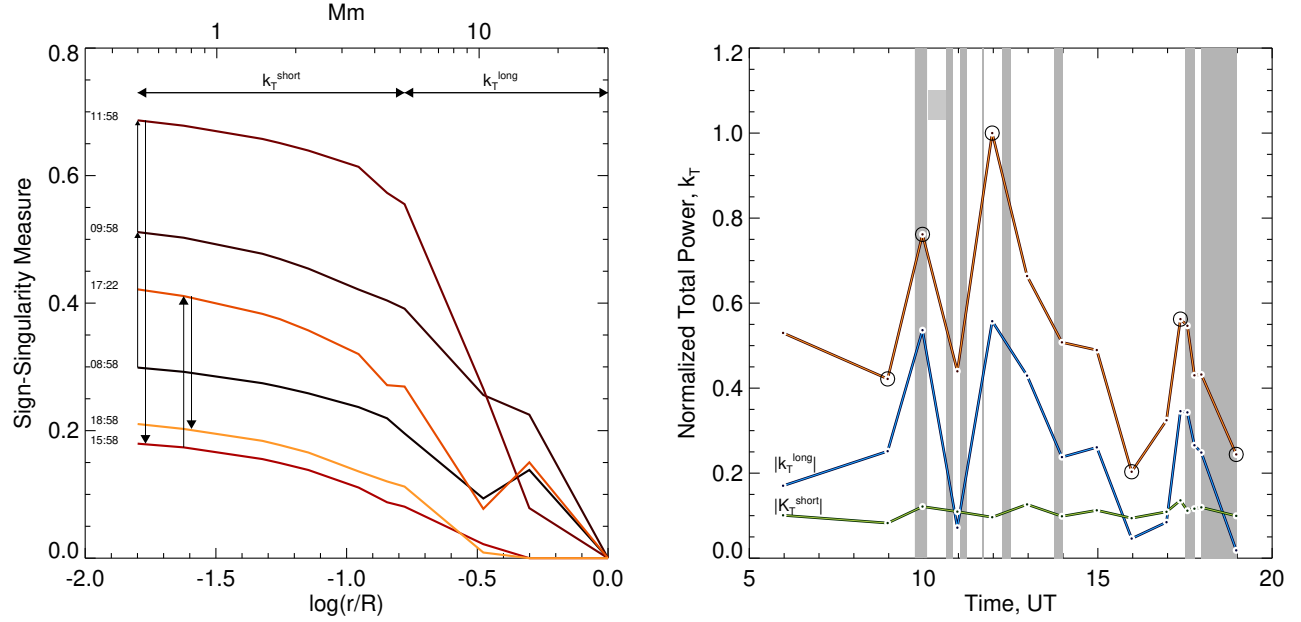


**Figure 7.** Sign-singularity measures (left, curves) shown for selected time instances, and time variations of their parameters (right) calculated for the twist maps shown in Fig. 4. In the left panel the arrows indicate direction of the evolution of these measures, while the time stamps are shown to connect these curves to the corresponding images in Fig. 4. The two-sided arrows mark linear intervals used to calculate the cancellation exponent,  $k_T^{short}$ , and the slope of the long range end of the measure,  $k_T^{long}$ . Right panel shows time variations of the total power (brown) calculated for each measure shown in the left panel, as well as the corresponding cancellation exponent ( $k_T^{short}$ , green) and the slope ( $k_T^{long}$ , blue). The data points indicated by circles are those that correspond to the measures in the left plot. The vertical strips indicate the start time and the duration of AIA 17.1 nm brightenings and the X1.2 flare (18:00-19:00 UT) associated with the AR filament and the horizontal bar between 10:07 and 10:37 UT marks the timing of a M7.2 flare that occurred in the south-east part of the AR.

all profiles may show weakly correlated general trends, the strong peaks in the cancellation exponents may not be explained by rapid changes in the observed flux profiles.

#### 4. DISCUSSION AND CONCLUSIONS

First, we summarize our main findings. Series of coronal field extrapolations suggest that i) the pre-eruption configuration of the AR included several MFR-like structures with twist exceeding 2; we detected a well defined MFRs only at the site of the future eruption; ii) the eruption was affected by overlying sunspot fields, which caused the ejecta to deflect side-wise at the initial stage; iii) slide-out eruptions may explain a large spread of the eruption threshold of the decay index; iv) the photospheric and the corresponding extrapolated fields are sensitive to energy build up and release processes; v) cancellation exponents calculated over the model twist data and the observed photospheric current helicity maps showed synchronous variations, which include pre-flare increase followed by a gradual decrease that begins with the flare onset.

Wang & Zhang (2007) found that confined, non-eruptive flares tend to originate from the magnetic center of ARs, while eruptive ones are more likely to erupt from the periphery of ARs. These results emphasise the role that overlying fields play in producing CMEs (see also Baumgartner et al. 2018). Panasenco et al. (2013) reported that during the eruption process the ejected magnetic fields are channeled towards weaker field, which facilitates their escape from the corona. Thus, coronal holes or sunspot fields may create unbalanced forces acting on ejecta (e.g., Gopalswamy et al. 2009) causing them to propagate in the non-radial direction along a path with least resistance, which is away from a coronal hole or a sunspot. On the other hand, magnetic fields of AR 11943, located immediately west of the studied AR, appear to be connected to the eruption site as evidenced by several initial flare brightening that occurred at the interface between the two ARs. It may be speculated that this pre-flare activity was a manifestation of reconnection processes that may have weakened the strapping fields and created favourable conditions for channeling and deflecting the resulting CME.



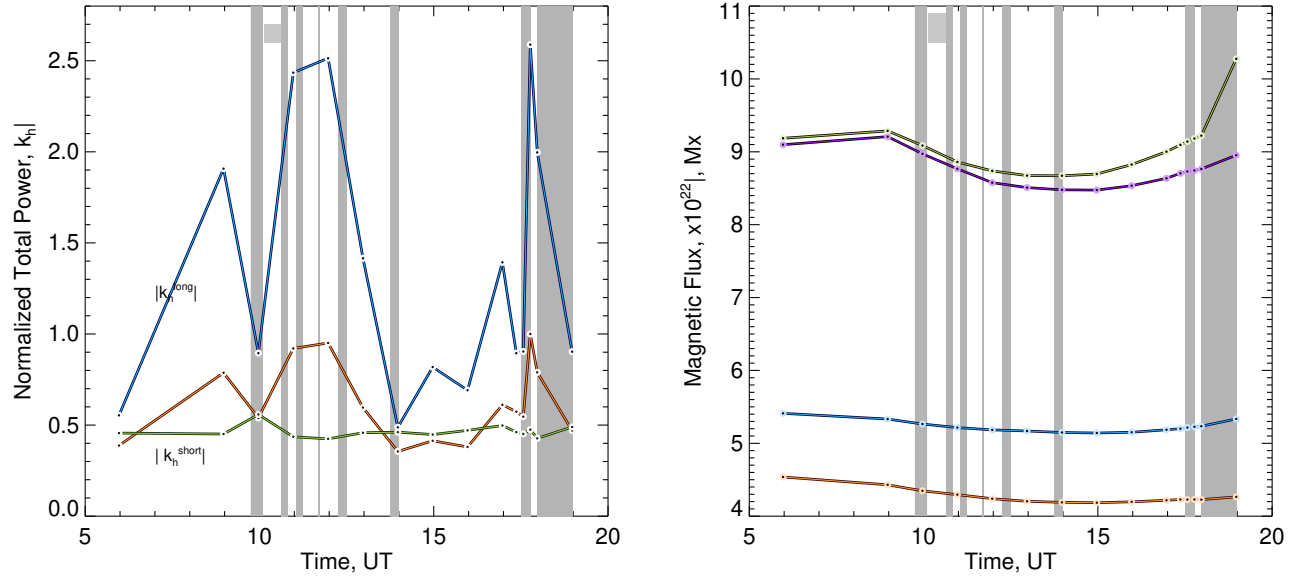


**Figure 8.** Left: Time variations of sign-singularity parameters calculated for current helicity maps obtained from observed vector magnetograms. The three curves show time variations of the total power (brown), the cancellation exponent ( $k_T^{short}$ , green), and the slope ( $k_T^{long}$ , blue). Right: Time variations of the magnitude of HMI magnetic flux calculated over the entire area shown in. Blue and orange profiles show data for northward and southward  $B_z$  component, while green and purple profiles represent horizontal  $B_x$  and  $B_y$  flux. In both panels the vertical strips indicate the start time and the duration of AIA 17.1 nm brightenings and the X1.2 flare (18:00-19:00 UT) associated with the AR filament, while the horizontal bar between 10:07 and 10:37 UT marks the timing of a M7.2 flare that occurred in the east part of the AR.

Very recently Kliem et al. (2021) arrived to a similar conclusion analyzing a height profile of a decay index calculated along an oblique propagation direction. In our case, the vertical decay index exceeded  $n = 1$  value only at heights above  $50''$ , which corresponded to the slanted sunspot fields, while the top of the large  $T_W$  structures reached heights of about  $35''$ . Although we did not calculate the oblique decay index, combination of the decay index profiles and twist maps allowed us to speculate that at heights above  $30''$  the decay index along the presumed propagation channel would decrease more rapidly thus facilitating the eruption process. It should be noted that earlier studies reported a wide range of the eruption threshold values,  $0.5 < n < 2$ , (e.g., Fan & Gibson 2007; Démoulin & Aulanier 2010; Olmedo & Zhang 2010; Zuccarello et al. 2015; Jing et al. 2018). The oblique eruption process, discussed above, may partially account for the wide range of eruption thresholds. Another possible reason is that the critical decay index was derived from a rather simple model. At the same time, the critical value is strongly dependent on the boundary conditions, aspect ratio of the MFR, other parameters (e.g., Alt et al. 2021). The MFR derived from our extrapolations represents a very complex structure and it is likely that lower values of the decay index are allowed as the critical value. For example, Inoue et al. (2016) concluded that if multiple MFR are present and some of them have the same helicity, then the pinch force will make the system more stable, which of course will modify the critical value of the decay index. Finally, Ishiguro & Kusano (2017) found that a double arc loop system may become unstable even if the external field does not decay with altitude. Thus the double arc instability (Ishiguro & Kusano 2017), being independent of the decay index may realize conditions for tether-cutting reconnection as an onset mechanism of solar eruptions.

Wang et al. (2015) analyzed the same AR as that studied here and argued that open field structures detected in their extrapolations could be a guide for the eruption fields (see also Möstl et al. 2015). Our extrapolations did not include open field lines at the site of the eruption, however, we note that Fleishman et al. (2019) concluded that the NLFFF extrapolation routine tends to produce a more “closed” magnetic field configuration as compared to the test data. We therefore speculate that the ejecta was non-radially escaping from underneath the extended sunspot fields, along a channel with a low decay index. Although details of our and Wang et al. (2015) extrapolations may differ, they both agree on the non-radial propagation of the ejecta and strong influence of the sunspot fields. We thus further confirm the important role that the large scale magnetic environment play in the low corona in defining the direction

of a magnetic eruption. An alternative explanation of the CME deflection may be a medium-sized coronal hole that was located approximately at 0.5 solar radii north-east of the AR. It is known that coronal hole may deflect CMEs (e.g., [Gopalswamy et al. 2009](#)), although this coronal hole appeared to be too far to have a dominant effect at the early stage of the eruption.

[Zheng et al. \(2016\)](#) suggested that the complex structure of the X1.2 flare in AR NOAA 11944 may result from a complex distribution of photospheric magnetic flux and that the eruption probably involved at least two magnetic reconnection events. These inferences are in accord with our model data, which show presence of several MFRs nested above the PIL. While we did not consider details of magnetic restructuring and possible changes in MFR footpoint connectivity that led to the eruption, it is safe to assume that eruption of these complex structures may, at least partially, explain the complex structure of flare emission. This is also in line with [Kliem et al. \(2021\)](#) arguments that an unstable MFR may be formed or enhanced by a series of confined flares prior to complete eruption. Its subsequent evolution toward an equilibrium state may explain the slow-rise stage of an ejecta. Here we would like to note that, according to the field extrapolations, significant changes in the corona of the AR commenced at approximately 17:46 UT, i.e., 15 min prior to the X1.2 flare onset. During this pre-flare activation period, various plasma flows and compact burst like brightenings were detected in AIA 17.1 nm data, while the impulsive phase of the eruption with enhanced emission began only after 18:00 UT. We may speculate that the pre-flare changes seen in the model field and driven by observed photospheric magnetograms may be the search of the equilibrium suggested by [Kliem et al. \(2021\)](#).

Pre-flare changes in the magnetic fields are also evident in the sign-singularity analysis that show enhancements of model twist and observed current helicity structures prior to the flare followed by their rapid exhaust during the pre-flare activation period. These findings are in agreement with our earlier studies based on data with lower spatial and temporal resolution, which indicated that current helicity distribution may rapidly change prior to a flare event ([Abramenko et al. 1998](#); [Yurchyshyn et al. 2000a, 2012](#)). Since the magnetic flux plots do not show any variations that would temporarily correlate with the cancellation exponents, we may suggest that the structural variations in the AR were mostly associated with enhancements of current systems (twist) in the AR rather than energy injection via new flux emergence.

According to the model data, strong twist structures developed in the AR corona within several hours prior to the eruption. It is not clear what was the driver of this pre-flare energy build up above the PIL. The eruption occurred at the periphery of the AR and HMI magnetograms did not show any evidence of new magnetic flux emerging in the area. The Q-maps in Figure 3 and the local correlation tracking technique indicated that there were converging motions toward the flaring PIL. We therefore speculate that the most likely mechanism responsible for the origin of the pre-flare MFR build-up detected in the model data is magnetic reconnection resulting from restructuring of the AR magnetic fields driven by the converging flows as well as the series of small flares east of the eruption site. Although this assumption agrees with the occurrence of multiple brightenings prior to the onset of the main flare, a in depth study and MHD simulations are needed to understand this process. It is also worth noting that this process may also be considered as condensation of magnetic helicity at PILs ([Antiochos 2013](#)). It is proposed that helicity is injected into the AR atmosphere by the continuous large and small-scale photospheric motions and flux emergence and it may then be cascading toward larger spatial scales. It is thus plausible that rapid formation of large twist structures seen in the extrapolated data are due to transfer of “pre-existing” helicity from small to large-scale structures via magnetic reconnection, which conserves the helicity present in a given domain ([Berger 1984](#)).

Finally, this study demonstrates that coronal models of AR magnetic fields may have a potential for predicting likelihood, location, and timing of solar flares. Thus, analysis of coronal configurations using available extrapolation tools (e.g., [Wiegmann et al. 2006](#); [Fleishman et al. 2017](#); [Fleishman et al. 2019](#); [Duan et al. 2019a](#)) and/or MHD modeling (e.g., [Cheung & DeRosa 2012](#); [Jiang & Feng 2012](#); [Inoue et al. 2014](#); [Jiang et al. 2016](#)) may reveal the existence and location of a MFR in an AR, while time profiles of various parameters describing magnetic fields structures may be utilized to study timing of ongoing evolution. Very recently, [Gupta et al. \(2021\)](#) studied relative magnetic helicity variations for a sample of ten ARs that produced large solar flares (GOES class > M1.0) using NLFFF extrapolations produced by [Wiegmann & Inhester \(2010\)](#) method. In particular they note that energy and helicity ratios derived from NLFFF data may allow to determine the potential of an AR to produce a CME.

## ACKNOWLEDGMENTS

We thank referees for careful reading the manuscript and providing valuable criticism and suggestions. BBSO operation is supported by NJIT and US NSF AGS-1821294 grants. GST operation is partly supported by the Korea Astronomy and Space Science Institute (KASI) and Seoul National University. This work was supported in part by NSF grants AST-1820613, AGS-1927578, AGS-1743321, and AGS-2121632, and NASA grants 80NSSC18K0667, 80NSSC19K0068, and 80NSSC20K0627 awarded to NJIT. V.Y. acknowledges support from NSF AST-1614457, AGS-1954737, AST-2108235, AFOSR FA9550-19-1-0040, NASA 80NSSC17K0016, 80NSSC19K0257, and 80NSSC20K0025 grants.

*Facilities:* SDO(AIA and HMI)

*Software:* gx\_simulator(Nita et al. 2015, 2018); Q-factor calculation package(Liu et al. 2016)

## REFERENCES

- Abramenko, V. I., Wang, T., & Yurchyshyn, V. 1996, SoPh, 168, 75, doi: [10.1007/BF00145826](https://doi.org/10.1007/BF00145826)
- Abramenko, V. I., Yurchyshyn, V., & Carbone, V. 1998, A&A, 334, L57
- Alt, A., Myers, C. E., Ji, H., et al. 2021, ApJ, 908, 41, doi: [10.3847/1538-4357/abda4b](https://doi.org/10.3847/1538-4357/abda4b)
- Antiochos, S. K. 2013, ApJ, 772, 72, doi: [10.1088/0004-637X/772/1/72](https://doi.org/10.1088/0004-637X/772/1/72)
- Antiochos, S. K., DeVore, C. R., & Klimchuk, J. A. 1999, The Astrophysical Journal, 510, 485, doi: [10.1086/306563](https://doi.org/10.1086/306563)
- Aulanier, G., Török, T., Démoulin, P., & DeLuca, E. E. 2010, ApJ, 708, 314, doi: [10.1088/0004-637X/708/1/314](https://doi.org/10.1088/0004-637X/708/1/314)
- Aulanier, G., Török, T., Démoulin, P., & DeLuca, E. E. 2009, The Astrophysical Journal, 708, 314, doi: [10.1088/0004-637x/708/1/314](https://doi.org/10.1088/0004-637x/708/1/314)
- Barnes, G., Leka, K. D., Schrijver, C. J., et al. 2016, The Astrophysical Journal, 829, 89, <http://stacks.iop.org/0004-637X/829/i=2/a=89>
- Baty, H. 2001, A&A, 367, 321, doi: [10.1051/0004-6361:20000412](https://doi.org/10.1051/0004-6361:20000412)
- Baumgartner, C., Thalmann, J. K., & Veronig, A. M. 2018, ApJ, 853, 105, doi: [10.3847/1538-4357/aaa243](https://doi.org/10.3847/1538-4357/aaa243)
- Berger, M. A. 1984, Geophysical and Astrophysical Fluid Dynamics, 30, 79, doi: [10.1080/03091928408210078](https://doi.org/10.1080/03091928408210078)
- Berger, M. A., & Prior, C. 2006, Journal of Physics A: Mathematical and General, 39, 8321, doi: [10.1088/0305-4470/39/26/005](https://doi.org/10.1088/0305-4470/39/26/005)
- Bobra, M. G., Sun, X., Hoeksema, J. T., et al. 2014, SoPh, 289, 3549, doi: [10.1007/s11207-014-0529-3](https://doi.org/10.1007/s11207-014-0529-3)
- Burlaga, L., Sittler, E., Mariani, F., & Schwenn, R. 1981, Journal of Geophysical Research: Space Physics, 86, 6673, doi: [10.1029/JA086iA08p06673](https://doi.org/10.1029/JA086iA08p06673)
- Chen, P. F., & Shibata, K. 2000, ApJ, 545, 524, doi: [10.1086/317803](https://doi.org/10.1086/317803)
- Cheung, M. C. M., & DeRosa, M. L. 2012, ApJ, 757, 147, doi: [10.1088/0004-637X/757/2/147](https://doi.org/10.1088/0004-637X/757/2/147)
- Démoulin, P., & Aulanier, G. 2010, ApJ, 718, 1388, doi: [10.1088/0004-637X/718/2/1388](https://doi.org/10.1088/0004-637X/718/2/1388)
- Duan, A., Jiang, C., He, W., et al. 2019a, ApJ, 884, 73, doi: [10.3847/1538-4357/ab3e33](https://doi.org/10.3847/1538-4357/ab3e33)
- . 2019b, ApJ, 884, 73, doi: [10.3847/1538-4357/ab3e33](https://doi.org/10.3847/1538-4357/ab3e33)
- Duan, A., Jiang, C., Zou, P., Feng, X., & Cui, J. 2021, ApJ, 906, 45, doi: [10.3847/1538-4357/abc701](https://doi.org/10.3847/1538-4357/abc701)
- Falconer, D. A., Moore, R. L., Barghouty, A. F., & Khazanov, I. 2014, Space Weather, 12, 306, doi: [10.1002/2013SW001024](https://doi.org/10.1002/2013SW001024)
- Falconer, D. A., Tiwari, S. K., Moore, R. L., & Khazanov, I. 2016, ApJL, 833, L31, doi: [10.3847/2041-8213/833/2/L31](https://doi.org/10.3847/2041-8213/833/2/L31)
- Fan, Y., & Gibson, S. E. 2003, ApJL, 589, L105, doi: [10.1086/375834](https://doi.org/10.1086/375834)
- Fan, Y., & Gibson, S. E. 2004, ApJ, 609, 1123, doi: [10.1086/421238](https://doi.org/10.1086/421238)
- Fan, Y., & Gibson, S. E. 2007, ApJ, 668, 1232, doi: [10.1086/521335](https://doi.org/10.1086/521335)
- Fleishman, G., Mysh'yakov, I., Stupishin, A., Loukitcheva, M., & Anfinogentov, S. 2019, ApJ, 870, 101, doi: [10.3847/1538-4357/aaf384](https://doi.org/10.3847/1538-4357/aaf384)
- Fleishman, G. D., Anfinogentov, S., Loukitcheva, M., Mysh'yakov, I., & Stupishin, A. 2017, The Astrophysical Journal, 839, 30, doi: [10.3847/1538-4357/aa6840](https://doi.org/10.3847/1538-4357/aa6840)
- Gopalswamy, N., Mäkelä, P., Xie, H., Akiyama, S., & Yashiro, S. 2009, Journal of Geophysical Research (Space Physics), 114, A00A22, doi: [10.1029/2008JA013686](https://doi.org/10.1029/2008JA013686)
- Gopalswamy, N., Yashiro, S., & Akiyama, S. 2007, Journal of Geophysical Research (Space Physics), 112, A06112, doi: [10.1029/2006JA012149](https://doi.org/10.1029/2006JA012149)
- Gosling, J. T., Bame, S. J., McComas, D. J., & Phillips, J. L. 1990, Geophys. Res. Lett., 17, 901, doi: [10.1029/GL017i007p00901](https://doi.org/10.1029/GL017i007p00901)



- Gupta, M., Thalmann, J. K., & Veronig, A. M. 2021, arXiv e-prints, arXiv:2106.08781.  
<https://arxiv.org/abs/2106.08781>
- Hood, A. W., & Priest, E. R. 1981, *Geophysical and Astrophysical Fluid Dynamics*, 17, 297,  
 doi: [10.1080/03091928108243687](https://doi.org/10.1080/03091928108243687)
- Inoue, S., Hayashi, K., & Kusano, K. 2016, *ApJ*, 818, 168,  
 doi: [10.3847/0004-637X/818/2/168](https://doi.org/10.3847/0004-637X/818/2/168)
- Inoue, S., Magara, T., Pandey, V. S., et al. 2014, *ApJ*, 780, 101, doi: [10.1088/0004-637X/780/1/101](https://doi.org/10.1088/0004-637X/780/1/101)
- Ishiguro, N., & Kusano, K. 2017, *ApJ*, 843, 101,  
 doi: [10.3847/1538-4357/aa799b](https://doi.org/10.3847/1538-4357/aa799b)
- Jiang, C., & Feng, X. 2012, *ApJ*, 749, 135,  
 doi: [10.1088/0004-637X/749/2/135](https://doi.org/10.1088/0004-637X/749/2/135)
- Jiang, C., Wu, S. T., Yurchyshyn, V., et al. 2016, *ApJ*, 828, 62, doi: [10.3847/0004-637X/828/1/62](https://doi.org/10.3847/0004-637X/828/1/62)
- Jing, J., Liu, C., Lee, J., et al. 2018, *ApJ*, 864, 138,  
 doi: [10.3847/1538-4357/aad6e4](https://doi.org/10.3847/1538-4357/aad6e4)
- Karpen, J. T., Antiochos, S. K., & DeVore, C. R. 2012, *The Astrophysical Journal*, 760, 81,  
 doi: [10.1088/0004-637x/760/1/81](https://doi.org/10.1088/0004-637x/760/1/81)
- Kliem, B., Lee, J., Liu, R., et al. 2021, *ApJ*, 909, 91,  
 doi: [10.3847/1538-4357/abda37](https://doi.org/10.3847/1538-4357/abda37)
- Kliem, B., & Török, T. 2006, *Physical Review Letters*, 96, doi: [10.1103/physrevlett.96.255002](https://doi.org/10.1103/physrevlett.96.255002)
- Kusano, K., Bamba, Y., Yamamoto, T. T., et al. 2012, *ApJ*, 760, 31, doi: [10.1088/0004-637X/760/1/31](https://doi.org/10.1088/0004-637X/760/1/31)
- Kusano, K., Iju, T., Bamba, Y., & Inoue, S. 2020, *Science*, 369, 587, doi: [10.1126/science.aaz2511](https://doi.org/10.1126/science.aaz2511)
- Leka, K. D., Park, S.-H., Kusano, K., et al. 2019a, *ApJS*, 243, 36, doi: [10.3847/1538-4365/ab2e12](https://doi.org/10.3847/1538-4365/ab2e12)
- . 2019b, *ApJ*, 881, 101, doi: [10.3847/1538-4357/ab2e11](https://doi.org/10.3847/1538-4357/ab2e11)
- Lemen, J. R., Title, A. M., Akin, D. J., et al. 2012, *SoPh*, 275, 17, doi: [10.1007/s11207-011-9776-8](https://doi.org/10.1007/s11207-011-9776-8)
- Liu, R., Kliem, B., Titov, V. S., et al. 2016, *ApJ*, 818, 148,  
 doi: [10.3847/0004-637X/818/2/148](https://doi.org/10.3847/0004-637X/818/2/148)
- Lu, Z., Cao, W., Jin, G., et al. 2019, *ApJ*, 876, 133,  
 doi: [10.3847/1538-4357/ab16d4](https://doi.org/10.3847/1538-4357/ab16d4)
- Marubashi, K., Akiyama, S., Yashiro, S., et al. 2015, *SoPh*, 290, 1371, doi: [10.1007/s11207-015-0681-4](https://doi.org/10.1007/s11207-015-0681-4)
- Moore, R. L., Sterling, A. C., Hudson, H. S., & Lemen, J. R. 2001, *The Astrophysical Journal*, 552, 833,  
 doi: [10.1086/320559](https://doi.org/10.1086/320559)
- Möstl, C., Rollett, T., Frahm, R. A., et al. 2015, *Nature Communications*, 6, 7135, doi: [10.1038/ncomms8135](https://doi.org/10.1038/ncomms8135)
- Nita, G. M., Fleishman, G. D., Kuznetsov, A. A., Kontar, E. P., & Gary, D. E. 2015, *ApJ*, 799, 236,  
 doi: [10.1088/0004-637X/799/2/236](https://doi.org/10.1088/0004-637X/799/2/236)
- Nita, G. M., Viall, N. M., Klimchuk, J. A., et al. 2018, *ApJ*, 853, 66, doi: [10.3847/1538-4357/aaa4bf](https://doi.org/10.3847/1538-4357/aaa4bf)
- Olmedo, O., & Zhang, J. 2010, *ApJ*, 718, 433,  
 doi: [10.1088/0004-637X/718/1/433](https://doi.org/10.1088/0004-637X/718/1/433)
- Ott, E., Du, Y., Sreenivasan, K. R., Juneja, A., & Suri, A. K. 1992, *PhRvL*, 69, 2654,  
 doi: [10.1103/PhysRevLett.69.2654](https://doi.org/10.1103/PhysRevLett.69.2654)
- Panasenco, O., Martin, S. F., Velli, M., & Vourlidas, A. 2013, *SoPh*, 287, 391, doi: [10.1007/s11207-012-0194-3](https://doi.org/10.1007/s11207-012-0194-3)
- Park, S.-H., Leka, K. D., Kusano, K., et al. 2020, *ApJ*, 890, 124, doi: [10.3847/1538-4357/ab65f0](https://doi.org/10.3847/1538-4357/ab65f0)
- Patsourakos, S., Vourlidas, A., Török, T., et al. 2020, *SSRv*, 216, 131, doi: [10.1007/s11214-020-00757-9](https://doi.org/10.1007/s11214-020-00757-9)
- Pesnell, W. D., Thompson, B. J., & Chamberlin, P. C. 2012, *SoPh*, 275, 3, doi: [10.1007/s11207-011-9841-3](https://doi.org/10.1007/s11207-011-9841-3)
- Pevtsov, A. A., & Canfield, R. C. 2001, *J. Geophys. Res.*, 106, 25191, doi: [10.1029/2000JA004018](https://doi.org/10.1029/2000JA004018)
- Pevtsov, A. A., Canfield, R. C., & Metcalf, T. R. 1994, *ApJL*, 425, L117, doi: [10.1086/187324](https://doi.org/10.1086/187324)
- Savcheva, A., Pariat, E., van Ballegooijen, A., Aulanier, G., & DeLuca, E. 2012, *The Astrophysical Journal*, 750, 15,  
 doi: [10.1088/0004-637x/750/1/15](https://doi.org/10.1088/0004-637x/750/1/15)
- Scherrer, P. H., Schou, J., Bush, R. I., et al. 2012, *SoPh*, 275, 207, doi: [10.1007/s11207-011-9834-2](https://doi.org/10.1007/s11207-011-9834-2)
- Schou, J., Scherrer, P. H., Bush, R. I., et al. 2012, *SoPh*, 275, 229, doi: [10.1007/s11207-011-9842-2](https://doi.org/10.1007/s11207-011-9842-2)
- Seehafer, N. 1994, *A&A*, 284, 593
- Sorriso-Valvo, L., Carbone, V., Veltri, P., et al. 2004a, *Planet. Space Sci.*, 52, 937, doi: [10.1016/j.pss.2004.02.006](https://doi.org/10.1016/j.pss.2004.02.006)
- . 2004b, *Planet. Space Sci.*, 52, 937,  
 doi: [10.1016/j.pss.2004.02.006](https://doi.org/10.1016/j.pss.2004.02.006)
- Sorriso-Valvo, L., De Vita, G., Kazachenko, M. D., et al. 2015, *ApJ*, 801, 36, doi: [10.1088/0004-637X/801/1/36](https://doi.org/10.1088/0004-637X/801/1/36)
- Srivastava, N., & Venkatakrisnan, P. 2004, *Journal of Geophysical Research (Space Physics)*, 109, A10103,  
 doi: [10.1029/2003JA010175](https://doi.org/10.1029/2003JA010175)
- Thompson, W. T. 2006, *A&A*, 449, 791,  
 doi: [10.1051/0004-6361:20054262](https://doi.org/10.1051/0004-6361:20054262)
- Titov, V. S. 2007, *ApJ*, 660, 863, doi: [10.1086/512671](https://doi.org/10.1086/512671)
- Titov, V. S., Hornig, G., & Démoulin, P. 2002, *Journal of Geophysical Research (Space Physics)*, 107, 1164,  
 doi: [10.1029/2001JA000278](https://doi.org/10.1029/2001JA000278)
- Toriumi, S., Schrijver, C. J., Harra, L. K., Hudson, H., & Nagashima, K. 2017a, *ApJ*, 834, 56,  
 doi: [10.3847/1538-4357/834/1/56](https://doi.org/10.3847/1538-4357/834/1/56)
- . 2017b, *ApJ*, 834, 56, doi: [10.3847/1538-4357/834/1/56](https://doi.org/10.3847/1538-4357/834/1/56)
- Toriumi, S., & Takasao, S. 2017, *ApJ*, 850, 39,  
 doi: [10.3847/1538-4357/aa95c2](https://doi.org/10.3847/1538-4357/aa95c2)
- Török, T., & Kliem, B. 2003, *A&A*, 406, 1043,  
 doi: [10.1051/0004-6361:20030692](https://doi.org/10.1051/0004-6361:20030692)
- . 2005, *ApJL*, 630, L97, doi: [10.1086/462412](https://doi.org/10.1086/462412)

- Tsurutani, B. T., Smith, E. J., Gonzalez, W. D., Tang, F., & Akasofu, S. I. 1988, *J. Geophys. Res.*, 93, 8519, doi: [10.1029/JA093iA08p08519](https://doi.org/10.1029/JA093iA08p08519)
- Török, T., & Kliem, B. 2005, *The Astrophysical Journal*, 630, L97, doi: [10.1086/462412](https://doi.org/10.1086/462412)
- Wang, R., Liu, Y. D., Dai, X., et al. 2015, *ApJ*, 814, 80, doi: [10.1088/0004-637X/814/1/80](https://doi.org/10.1088/0004-637X/814/1/80)
- Wang, Y., & Zhang, J. 2007, *ApJ*, 665, 1428, doi: [10.1086/519765](https://doi.org/10.1086/519765)
- Wheatland, M. S., Sturrock, P. A., & Roumeliotis, G. 2000, *ApJ*, 540, 1150, doi: [10.1086/309355](https://doi.org/10.1086/309355)
- Wiegmann, T. 2004, *SoPh*, 219, 87, doi: [10.1023/B:SOLA.0000021799.39465.36](https://doi.org/10.1023/B:SOLA.0000021799.39465.36)
- Wiegmann, T., & Inhester, B. 2010, *A&A*, 516, A107, doi: [10.1051/0004-6361/201014391](https://doi.org/10.1051/0004-6361/201014391)
- Wiegmann, T., Inhester, B., & Sakurai, T. 2006, *SoPh*, 233, 215, doi: [10.1007/s11207-006-2092-z](https://doi.org/10.1007/s11207-006-2092-z)
- Yardley, S. L., Mackay, D. H., & Green, L. M. 2021, *SoPh*, 296, 10, doi: [10.1007/s11207-020-01749-2](https://doi.org/10.1007/s11207-020-01749-2)
- Yashiro, S., Gopalswamy, N., Michalek, G., et al. 2004, *Journal of Geophysical Research (Space Physics)*, 109, A07105, doi: [10.1029/2003JA010282](https://doi.org/10.1029/2003JA010282)
- Yurchyshyn, V., Abramenko, V., & Watanabe, H. 2012, in *Astronomical Society of the Pacific Conference Series*, Vol. 454, *Hinode-3: The 3rd Hinode Science Meeting*, ed. T. Sekii, T. Watanabe, & T. Sakurai, 311
- Yurchyshyn, V., Abramenko, V. I., & Carbone, V. 2000a, *ApJ*, 538, 968, doi: [10.1086/309139](https://doi.org/10.1086/309139)
- Yurchyshyn, V., Hu, Q., & Abramenko, V. I. 2005, *Space Weather*, 3, 8, doi: [10.1029/2004SW000124](https://doi.org/10.1029/2004SW000124)
- Yurchyshyn, V., Wang, H., & Abramenko, V. I. 2004, *Space Weather*, 2, 2001, doi: [10.1029/2003SW000020](https://doi.org/10.1029/2003SW000020)
- Yurchyshyn, V. B., Abramenko, V. I., & Carbone, V. 2000b, *ApJ*, 538, 968, doi: [10.1086/309139](https://doi.org/10.1086/309139)
- Zhang, J., Richardson, I. G., Webb, D. F., et al. 2007, *Journal of Geophysical Research (Space Physics)*, 112, A10102, doi: [10.1029/2007JA012321](https://doi.org/10.1029/2007JA012321)
- Zhang, J., Richardson, I. G., Webb, D. F., et al. 2007, *Journal of Geophysical Research: Space Physics*, 112, n/a, doi: [10.1029/2007JA012321](https://doi.org/10.1029/2007JA012321)
- Zheng, R., Chen, Y., & Wang, B. 2016, *ApJ*, 823, 136, doi: [10.3847/0004-637X/823/2/136](https://doi.org/10.3847/0004-637X/823/2/136)
- Zuccarello, F. P., Aulanier, G., & Gilchrist, S. A. 2015, *ApJ*, 814, 126, doi: [10.1088/0004-637X/814/2/126](https://doi.org/10.1088/0004-637X/814/2/126)